Influence Analysis of Impeller-Guide Vane Matching on Energy and Pressure Pulsation in a Tubular Pump Device

Z. Lin[1], F. Yang[1,2†], X. Xu[3], X. Jin[1], M. Chen[2,4] and G. Xu[2]

[1] *College of Hydraulic Science and Engineering, Yangzhou University, Yangzhou, Jiangsu, 225009, China*
[2] *Jiangsu Provincial Key Laboratory of Water Conservancy and Power Engineering, Yangzhou, Jiangsu, 225009, China*
[3] *Jiangsu Hydraulic Research Institute, Nanjing, Jiangsu, 210029, China*
[4] *Huaian Water Conservancy Survey and Design, Huaian, Jiangsu, 223005, China*

†*Corresponding Author Email: fanyang@yzu.edu.cn*

ABSTRACT

Tubular pump devices offer advantages such as low hydraulic losses, a simple structure, and easy maintenance. They find extensive application in areas such as irrigation, flood control, and water diversion. The performance and security of the pump are directly impacted by the contact between the impeller and guide vane. The matching relationship between the number of impeller blades and guide vanes significantly influences this interaction in tubular pump devices. To explore this impact, a Very-Large-Eddy Simulation turbulence model was employed to simulate the 3D flow fields of six different number matching relationships in a shaft tubular pump device. The analysis focused on the energy performance of the different schemes, the flow distribution of the guide vanes, and the velocity circulation at the guide vanes' outlet. Entropy theory and energy gradient theory were employed to understand how the number matching relationship influences energy performance. Additionally, pressure pulsations were analyzed at the impeller and guide vanes for different matching configurations. The results indicate that although increasing the number of impeller blades can lead to higher water circulation, increased energy, and potentially unstable water flow, an increase in impeller blades number results in improved flow distribution in each guide vane groove, leading to an overall enhancement in the efficiency of the pump device. Similarly, increasing the number of guide vanes may increase the non-uniformity of the guide vane flow rate, but it also enhances the ability of the guide vanes to regulate water circulation and recover energy, thereby benefiting the overall efficiency.

1. INTRODUCTION

Shaft tubular pumps belong to the category of low lift and high flow centrifugal pumps. They offer several advantages, including straight inlet and outlet pipes, minimal hydraulic losses, simple and compact unit structures, and easy management and maintenance. As a result, they are used in China for agricultural irrigation, flood control, and regional water diversion. Notable examples of shaft tubular pump installations in China include the Meiliang Lake Pump Station, Jiangjie Pump Station, and Guangling East Hub Pump Station in Jiangsu Province. These pump stations have adopted shaft tubular pump devices.

The impeller (IMP) and guide vane (GV) are crucial components of the shaft tubular pump device as they directly impact the overall performance. The IMP converts mechanical energy into kinetic energy. As water passes through the rotating blades of the IMP, its uniformity and stability are disrupted, leading to a significant increase in velocity. The GVs then recover the velocity circulation of the water exiting the IMP, converting kinetic energy into pressure, and effectively guiding the water into the outlet pipe, thereby reducing hydraulic losses.

The contact between the high-speed IMP and stationary GV in the pump's flow field is known as rotor-stator interaction. This interaction generates periodic pressure pulsations at the junction of the IMP and GV (Yan et al., 2010; Nicolet et al., 2010; Zhang et al., 2016; Trivedi, 2018), resulting in hydraulic vibration and propaginating in the flow direction. The pressure

Nomenclature

Co	Courant number	Q	flow rate of pump device, m³/s
C_p	pressure coefficient	Qi	flow rate through a single guide vane groove, m³/s
DNS	Direct Numerical Simulation	RANS	Reynolds-averaged Navier-Stokes
D	nominal diameter of the impeller, mm	$\overline{Q_i}$	average flow rate through each blade groove
E	total pressure of the fluid, Pa	r^*	grid refinement factor
EGR	entropy generation rate	$\dot{S}_D^{'''}$	main flow entropy production rate
fi^*	solution of mesh convergence parameters	$\dot{S}_{D'}^{'''}$	turbulent dissipation entropy production rate
g	acceleration of gravity, N/kg	$\dot{S}_{\overline{D}}^{'''}$	time-average entropy production rate
GV	guide vane	s	flow line direction of fluid flow
H	Head of pump device, m	T	Kelvin temperature, K
H'	loss of mechanical energy along the flow line direction, J	Δt	time step, s
IMP	impeller	U	combined velocity of the three velocity components, m³/s
K	energy gradient function	U'	non-uniformity of flow
k	turbulent kinetic energy, J	VLES	Very-Large-Eddy Simulation
LES	Large Eddy Simulation	v	velocity, m/s
L_c	turbulence length scale, m	$|\overline{v}|$	absolute value of the estimated average velocity, m/s
L_i	integral length scale, m	x	Cartesian coordinate direction component
L_k	kolmogorov scale	ε	relative error
l	minimum size of the grid, m	η	efficiency, %
n	normal direction of fluid flow	μ	dynamic viscosity, m²/s
N	number of grid cells	μ_{eff}	effective dynamic viscosity, m²/s
P	instantaneous pressure, Pa	μ_t	turbulent viscosity, Pa·s
PPS	pressure pulsation signal	ρ	density of the fluid, kg/m³
$\overline{P}$	average pressure, Pa	ω	turbulent dissipation rate
p^*	convergence order		

pulsations also extend upstream along the IMP in the reverse flow direction, giving rise to phenomena such as jet flow, backflow, secondary flow, and flow separation. These phenomena significantly affect the pump's performance. If the frequency of pressure pulsations induced by rotor-stator interaction aligns with or is close to the natural frequency of the unit, it can cause system resonance in the pump device (Li et al., 2020). This resonance can result in fatigue damage to the IMP and GV and other flow-through components, posing a serious threat to the operation of the unit (Ohashi et al., 1994). Therefore, the rotor-stator interaction between the IMP and GV is vital for achieving high efficiency, consistent performance, and dependability in shaft tubular pumps. The blade number matching relationship between the IMP and GV is a key factor influencing the rotor-stator interaction characteristics. To enhance the hydraulic performanc and ensure the stable operation of the unit, it is necessary to examine how the blade number of the IMP and GV affects the rotor-stator interaction characteristics.

Several scholars have conducted studies on the blade number matching relationship between the IMP and GV in pump devices. For instance, Zhang et al. (2015) investigated the interference zone between the IMP and GV using the PIV test. Li et al. (2022a) examined the compatibility of the IMP and GV in seawater desalination pumps. Yan et al. (2022) and other researchers (Xu et al., 2020; Han et al., 2021) explored the impact of GV angle on hydraulic performance. Li et al. (2022b) and Lu et al. (2022) investigated the influence of GV shape on the flow field and pump efficiency. Al-Obaidi (2020) studied the impact of GVs on flow fields under unsteady flow conditions. Current research on shaft tubular pump devices includes optimization of pipe structure design (Yang et al., 2014; Xie et al., 2015) and investigations into flow field and internal flow characteristics of pump devices (Wang et al., 2017). Some scholars have also studied the impact of IMP and GV on the energy efficiency of pump devices (Pei et al., 2016; Meng et al., 2017; Jiao et al., 2021; Cheng et al., 2022; Xu et al., 2022). However, existing research is mainly focused on exploring the effect of IMP and GV design, including angling and contour, on energy efficiency, and there is limited analysis of the flow field from an energy perspective. Research on the impact of blade number matching relationship between the IMP and GV on the rotor-stator interaction characteristics in the pump is relatively scarce.

This study utilized the Very-Large-Eddy Simulation (VLES) model to perform numerical simulations of the shaft tubular pump device. The accuracy of the numerical
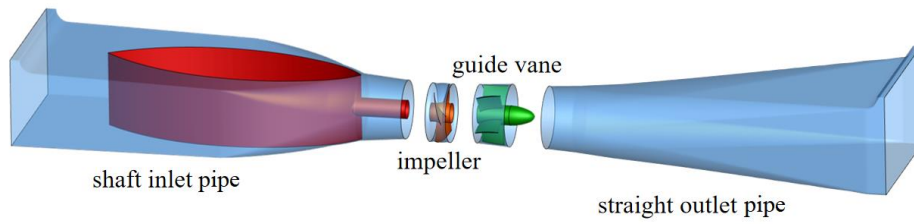
Fig. 1 3D model of shaft tubular pump device
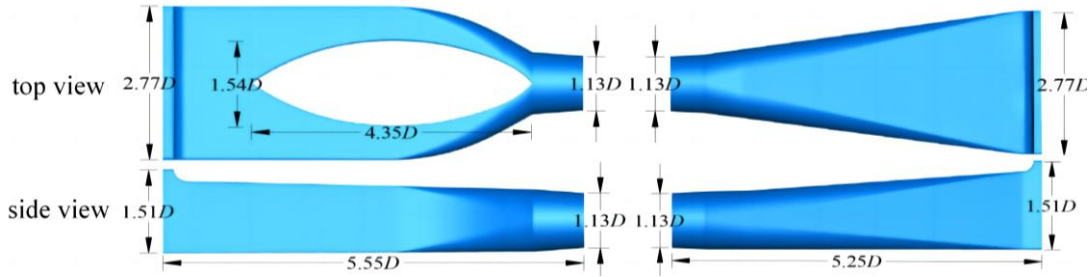
**Fig. 2 The main control size diagram of the pipes**

simulation was validated by comparing it with experimental data, and variations in the energy performance were observed under different blade number matching relationships between the IMP and GV. The study examined factors influencing the changes in pump device performance, such as GV flow non-uniformity and GV outlet velocity circulation. Entropy theory and energy gradient theory were employed to further elucidate the impact of blade number matching relationships on the internal flow field of the IMP and GV. Fast Fourier transform analysis was used to explore the time-frequency characteristics of pressure pulsation signals (PPS) of the IMP and GV and to investigate the influence of the IMP and GV blade number matching relationship on the rotor-stator interaction characteristics in the pump. This study can assist designers in enhancing the pump devices' hydraulic performance while ensuring their stability during operation and maintenance.

2. NUMERICAL MODEL AND THEORETICAL ANALYSIS

2.1 Calculation Model and Parameters

As illustrated in Fig. 1, the numerical calculations in this paper focused on a shaft tubular pump device, comprising four flow-through components. The IMP had a nominal diameter (D) of 300 mm. The blade installation angle was set at 0°. The IMP operated at a rated speed (n) of 981 r/min. The blade tip clearance width was 0.2 mm. The blade number matching relationship between the IMP and GV was achieved by axially separating them by 0.18D.

Based on the IMP's nominal diameter D, the main geometric dimensions of the shaft inlet pipe and straight outlet pipe are converted to dimensionless values. The key dimensions of the pipes are illustrated in Fig. 2. The shaft inlet pipe has a length of 5.55D, an inlet surface width of 2.77D, an inlet surface height of 1.51D, an
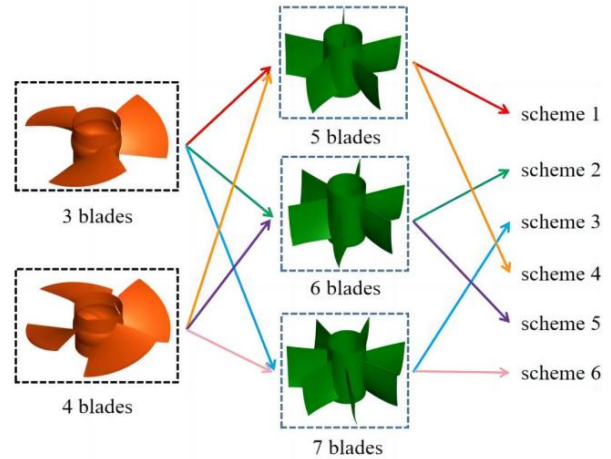
Fig. 3 Calculation schemes of IMP and GV matching

outlet surface diameter of 1.13D, a shaft length of 4.35D, and a shaft width of 1.54D. The straight outlet pipe has a length of 5.25D, an outlet width of 2.77D, an outlet height of 1.51D, and an inlet surface diameter of 1.13D.

Six schemes are considered with three and four IMP blades and five, six, and seven GV blades. The calculation schemes for the GV matching are presented in Fig. 3.

2.2 Numerical Model and Calculation Conditions

Assuming the fluid inside the pump device is an incompressible liquid and neglecting heat exchange, the fluid flow can be solved using Eqs. (Yan et al., 2022):

$$\frac{\partial \rho}{\partial t} + \nabla \cdot (\rho \mathbf{v}) = 0 \tag{1}$$

$$\frac{\partial \mathbf{v}}{\partial t} + (\mathbf{v} \cdot \nabla)\mathbf{v} = f_i - \frac{1}{\rho}\nabla p + v\nabla^2 \mathbf{v} \tag{2}$$

Table 1 Boundary condition

Boundary domain	Condition	Value
inlet	Relative pressure	1 atm
outlet	Mass flow	150–260 kg/s
solid wall surface	Non-slip boundary	
impeller zone of dynamic-static transition (steady)	Frozen Rotor	
impeller zone of dynamic-static transition (unsteady)	Transient Rotor Stator	
convergence accuracy		1.0×10^{-5}

where ρ is the fluid density, t is time, v is the velocity vector, and f_i is the mass force acting on the fluid.

Reynolds-averaged Navier-Stokes (RANS) models are widely utilized in engineering simulations and calculations of water flow due to their good convergence and reasonable calculation accuracy. These models have demonstrated their capability to reasonably simulate water flow in various engineering scenarios. However, they still have limitations when dealing with flows characterized by large streamline curvature and time scales (Zhao et al., 2021).

To address the deficiencies of RANS models while avoiding excessive computational resource consumption associated with large eddy simulation (LES) models, the VLES model has emerged as a hybrid turbulence model. The VLES model employs the RANS model to compute water flow near the wall surface. By introducing the control function F_r, the VLES model achieves a transition from DNS (direct numerical simulation) to RANS in the main flow region, enabling higher-precision simulations with fewer computational grids. Equation (1) presents the transport Eqs. for turbulent kinetic energy (k) and turbulent dissipation rate (ω) in the VLES model (Zhao et al., 2021).

$$\begin{cases} \dfrac{\partial k}{\partial t} + u_j \dfrac{\partial k}{\partial x_j} = \dfrac{\partial}{\partial x_j}\left[\left(v + \dfrac{\mu_t^{VLES}}{\sigma_K}\right)\dfrac{\partial k}{\partial x_j}\right] + P_k - \beta' k\omega \\[3mm] \dfrac{\partial \omega}{\partial t} + u_j \dfrac{\partial \omega}{\partial x_j} = \dfrac{\partial}{\partial x_j}\left[\left(v + \dfrac{\mu_t^{VLES}}{\sigma_\omega}\right)\dfrac{\partial \omega}{\partial x_j}\right] + \alpha\dfrac{\omega}{k}P_k - \beta_1\omega^2 \\[3mm] + 2(1 - F_1)\dfrac{1}{\sigma_{\omega 2}\omega}\dfrac{\partial k}{\partial x_j}\dfrac{\partial \omega}{\partial x_j} \end{cases} \quad (1)$$

where u is the velocity component, P_k is the turbulent kinetic energy generated by the laminar velocity gradient, F_1 is the control function, F_1 is taken as 1 in the near wall region, and 0 in the external and free shear flow regions. σ_K, σ_ω, β' and α are constant terms.

In particular, the turbulent viscosity μ_t is determined by (Zhao et al., 2021):

$$\mu_t^{VLES} = F_r \cdot \mu_t^{RANS} = F_r \cdot \rho k / \omega \quad (2)$$

$$F_r = \min\left(1.0, \left[\frac{1.0 - \exp\left(-\beta L_c / L_k\right)}{1.0 - \exp\left(-\beta L_i / L_k\right)}\right]^n\right) \quad (3)$$

$$L_c = C_x \left(\Delta_x \Delta_y \Delta_z\right)^{\frac{1}{3}} \quad (4)$$

$$L_i = k^{\frac{3}{2}} / \left(\beta_1^* k\omega\right) \quad (5)$$

$$L_k = v^{\frac{3}{4}} / \left(\beta_1^* k\omega\right)^{\frac{1}{4}} \quad (6)$$

$$C_x = \sqrt{0.3}C_s / \beta_1^* \quad (7)$$

$$C_s = \sqrt{\frac{\left[\left(C_{s,0}^2 \Delta^2 |S|^2\right) + v^2\right]^{1/2} - v}{\Delta^2 |S|}} \quad (8)$$

$$\Delta = \left(\Delta_x \Delta_y \Delta_z\right)^{\frac{1}{3}} \quad (9)$$

where Δ is the mesh scale, L_k, L_i, and L_c represent the Kolmogorov scale, integral length scale, and turbulence length scale, respectively. Model constants n, β, and β_1^* have values of 2, 0.09, and 0.002, respectively.

In this study, the fluid and solid regions are constrained using the wall boundary condition, with the solid wall set as a non-slip boundary. The General-Grid-Interface grid splicing technology is employed at the interfaces. The calculation boundary conditions were set according to the reference (Yang et al., 2022) for steady-state calculations to ensure accurate simulation results,. The specific settings are detailed in Table 1.

The time step establishes the interval between two successive flow field calculations in unsteady simulations. It dictates the duration and temporal resolution of the unsteady time advancement and has a substantial impact on the stability and accuracy of the calculation. Consequently, for a given computational grid, the time step must satisfy the stability condition, specifically the requirement of the Courant number, as follows:

$$Co = \frac{|\bar{v}|\Delta t}{l} \leq 1 \quad (10)$$

where $|\bar{v}|$ represents the estimated average velocity in absolute terms, where l is the minimum size of the grid.

According to the Nyquist theorem ($f_{s.max} \geq 2f_{max}$), the maximum frequency of a signal is generally taken as 2.56 to 4 times the frequency range. When the blade number is 3, the blade frequency is 49.05 Hz. To monitor PPS at twice the blade frequency, the maximum time step size Δt is determined as 3.3979×10^{-3} s. When the number of blades is 4, the time step Δt reaches a maximum of 1.9113×10^{-3} s. Taking all factors into consideration, the IMP calculation occurs once every 3° rotation, and the time step Δt is chosen as 5.09684×10^{-4} s.

2.3 Entropy Theory

Entropy production in a fluid system during operation is unavoidable, according to the second law of thermodynamics. In the case of water flow within the pump device, the existence of Reynolds stress and water viscosity leads to dissipative effects caused by irreversible factors. Fluid viscous forces convert kinetic and pressure energies into internal energy, and unstable flow phenomena such as vortices and backflows contribute to hydraulic losses, which are accompanied by an increase in entropy (Bejan, 1978; Kock & Herwig, 2005). Therefore, entropy generation can be a useful measure of the magnitude of hydraulic losses.

In turbulent flow, the entropy generation rate (EGR) of the fluid can be divided into two parts: one arising from time-averaged motion and the other from turbulent energy dissipation due to pulsating velocities. By employing Reynolds time averaging, Herwig and Kock (2006, 2007) derived Eqs. to calculate entropy generation per unit volume for time-mean and pulsating flow fields. The Eq. to calculate the EGR from time-averaged motion (direct dissipation) in a pump is given by (Kock & Herwig, 2005):

$$S_{\overline{D}}^{\prime\prime\prime} = \frac{2\mu_{eff}}{T}\left[\left(\frac{\partial \overline{u_1}}{\partial x_1}\right)^2 + \left(\frac{\partial \overline{u_2}}{\partial x_2}\right)^2 + \left(\frac{\partial \overline{u_3}}{\partial x_3}\right)^2\right]$$
$$+ \frac{\mu_{eff}}{T}\left[\left(\frac{\partial \overline{u_2}}{\partial x_1} + \frac{\partial \overline{u_1}}{\partial x_2}\right)^2 + \left(\frac{\partial \overline{u_2}}{\partial x_3} + \frac{\partial \overline{u_3}}{\partial x_2}\right)^2 + \left(\frac{\partial \overline{u_3}}{\partial x_1} + \frac{\partial \overline{u_1}}{\partial x_3}\right)^2\right] \quad (11)$$

The rate of entropy generation (referred to as turbulent dissipation entropy generation) in a pump device resulting from turbulent energy dissipation caused by pulsating velocity can be given by following Eqs. (Kock & Herwig, 2005):

$$S_{D'}^{\prime\prime\prime} = \frac{2\mu_{eff}}{T}\left[\left(\frac{\partial u_1'}{\partial x_1}\right)^2 + \left(\frac{\partial u_2'}{\partial x_2}\right)^2 + \left(\frac{\partial u_3'}{\partial x_3}\right)^2\right]$$
$$+ \frac{\mu_{eff}}{T}\left[\left(\frac{\partial u_2'}{\partial x_1} + \frac{\partial u_1'}{\partial x_2}\right)^2 + \left(\frac{\partial u_2'}{\partial x_3} + \frac{\partial u_3'}{\partial x_2}\right)^2 + \left(\frac{\partial u_3'}{\partial x_1} + \frac{\partial u_1'}{\partial x_3}\right)^2\right] \quad (12)$$

$$\mu_{eff} = \mu + \mu_t \quad (13)$$

where μ_{eff}, μ, and μ_t is the effective dynamic viscosity, dynamic viscosity, and turbulent viscosity, respectively.

The main flow EGR in the pump device caused by turbulent flow can be expressed by Eq. (Kock & Herwig, 2005):

$$S_D^{\prime\prime\prime} = S_{\overline{D}}^{\prime\prime\prime} + S_{D'}^{\prime\prime\prime} \quad (14)$$

where the turbulent dissipation EGR cannot be calculated directly. For sufficiently high Reynolds numbers, the EGR from turbulent dissipation follows this Eq. (Kock & Herwig, 2005):

$$S_{D'}^{\prime\prime\prime} = \frac{\rho\varepsilon}{T'} \quad (15)$$

where ε is the turbulent energy dissipation rate.

2.4 Energy Gradient Theory

The energy gradient method is a novel approach for investigating flow instability and turbulent rotation issues is the energy gradient theory (Dou, 2006; Dou et al., 2008) and provides an Eq. for the energy gradient function *K*, as proposed by Dou (2006):

$$K = \frac{\partial E / \partial n}{\partial H' / \partial s} \quad (16)$$

where *E* is the total pressure of the fluid, *H'* is the loss of mechanical energy along the flow line direction, *n* is the normal direction of fluid flow, and *s* is the flow line direction of fluid flow.

In a tubular pump device, the Eq. for the *K* of water flow is as follows (Dou, 2006):

$$K = \frac{\dfrac{\partial p}{\partial n} + \rho U \dfrac{\partial U}{\partial n}}{\dfrac{\mu}{U}\left(\dfrac{\partial U}{\partial n}\right)^2 - \dfrac{2\mu}{\rho U^2}\cdot\dfrac{\partial U}{\partial n}\cdot\dfrac{\partial p}{\partial n} + \dfrac{\mu}{\rho^2 U^3}\cdot\left(\dfrac{\partial p}{\partial n}\right)^2} \quad (17)$$

where *U* is the combined velocity of the three velocity components x, y, and z, *ρ* is the density of the fluid, and *μ* is the dynamic viscosity.

3. EFFECTIVENESS AND RELIABILITY ANALYSIS OF NUMERICAL SIMULATION

### 3.1 Computing Domain Grid Generation and Verification

Structured grids offer several advantages over unstructured grids, including faster generation, higher quality, and better representation of physical structures. Therefore, the pipes are separated into hexahedral structured grids. IMP and GV grids are generated by TurboGrid. The IMP adopts H/J/L grid topology, while the GV adopts H grid topology. The boundary layer position of the flow passage components and the gap area between the IMP blade tip are refined as illustrated in Fig. 4. The determinant of the calculation grid for the vertical shaft inlet pipe and the straight outlet pipe is both greater than 0.4. Table 2 presents the quality parameters of the calculation grid for the IMP and GV. Under the optimal working condition, the average y+ of the calculation grids for each component are all below 55, with the average y+ for the IMP and GV not exceeding 20. The average y+ values for each surface of the IMP and GV in scheme 1 under the optimal operating condition are shown in Fig. 5.

In Table 2, the face angle refers to the angle between the two edges of a face that intersect at a node and can be considered as a measure of skewness. The ratio of a face's longest edge to its shortest edge is known as the edge length ratio.Element Volume Ratio is defined as the ratio of the maximum volume of an element that touches a node, to the minimum volume of an element that touches a node.

In numerical simulations, the quality of the grid has a significant impact on both calculation speed and result
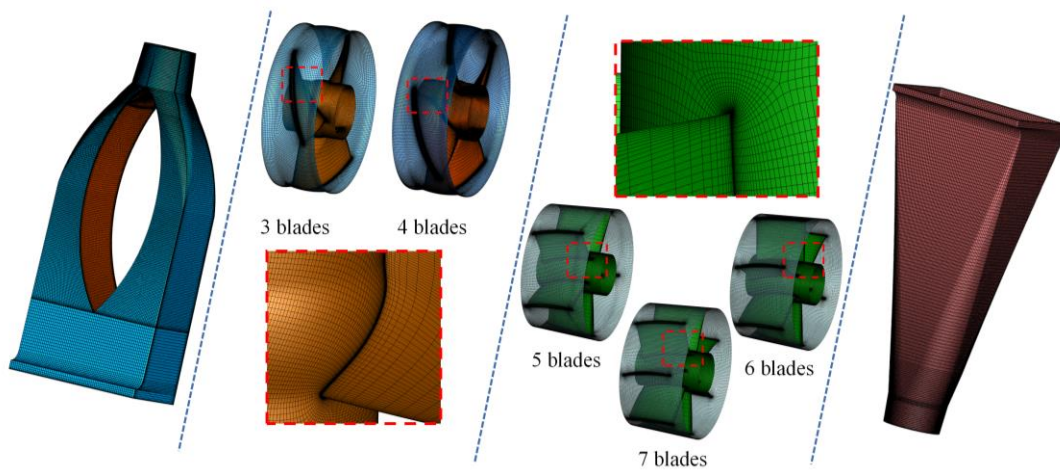
Fig. 4 Pump device grid
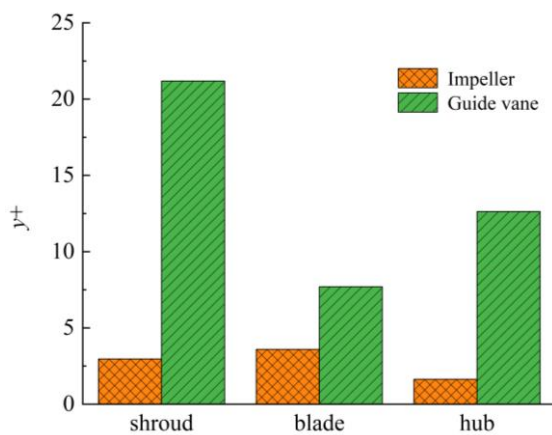
**Fig. 5 Average y+ of each surface of the IMP and GV (scheme 1)**

Table 2 The grid quality parameters for the IMP and GV.

Type	Impeller	Guide vane
Minimum face angle	29.3°	41.4°
Maximum face angle	161.4°	144.3°
Maximum element volume ratio	17.3	6.8
Maximum edge length ratio	385.3	242.4

accuracy. The type and division method of the grid also influence result accuracy. To strike a balance between numerical accuracy and computational efficiency, it is essential to establish grid independence and confirm convergence in the computational domain. In this study, scheme 1 with the fewest grid number (three IMP blades and five GVs) was selected as the subject for grid independence and convergence analysis. Seven sets of computational grids with different grid numbers were chosen under the optimal condition, and the corresponding pump device efficiency was compared and analyzed, as shown in Fig. 6. As the grid number increases, the pump efficiency stabilizes. When the grid reaches 5.1 million, the changes in pump efficiency do not exceed 0.1%, which satisfies the simulation's accuracy criteria (Yang et al., 2022).

To confirm grid convergence, the Richardson extrapolation method-based Grid Convergence Index (GCI) criterion was utilized. Three sets of grids, namely $N_1 = 3160844$, $N_2 = 4501681$, and $N_3 = 6483437$, were selected for discrete error analysis of pump device efficiency under optimal conditions. The calculated parameters are presented in Table 3. The calculated GCI_{12} and GCI_{23} were 0.280% and 0.053%, respectively, both below 1%. This indicates that the discrete errors of each grid scheme remained within the acceptable range (Yang et al., 2022). The grid convergence condition was
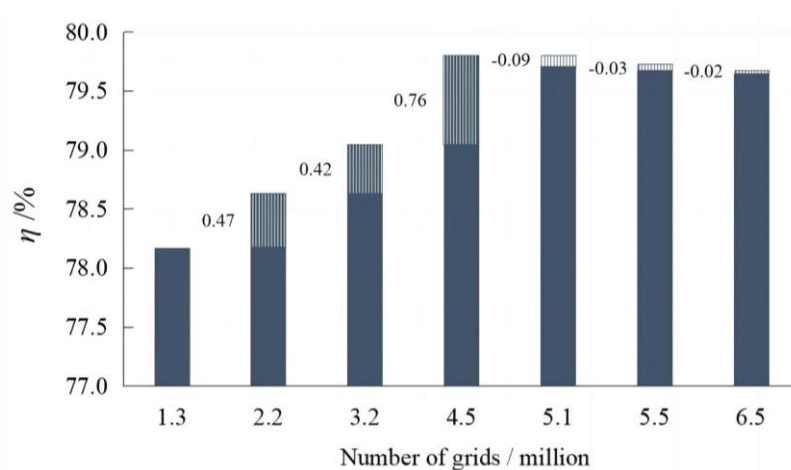
Fig. 6 Efficiency of pump device with different grid quantities (optimal condition)

Table 3 Grid GCI calculation result.

Number of grid cells N_i	r	$p*$	f_i	relative error ε / %	GCI / %
3160844			79.05		
4501681	1.125	14.2	79.80	−0.95	0.280
6483437	1.129		79.65	0.19	0.053
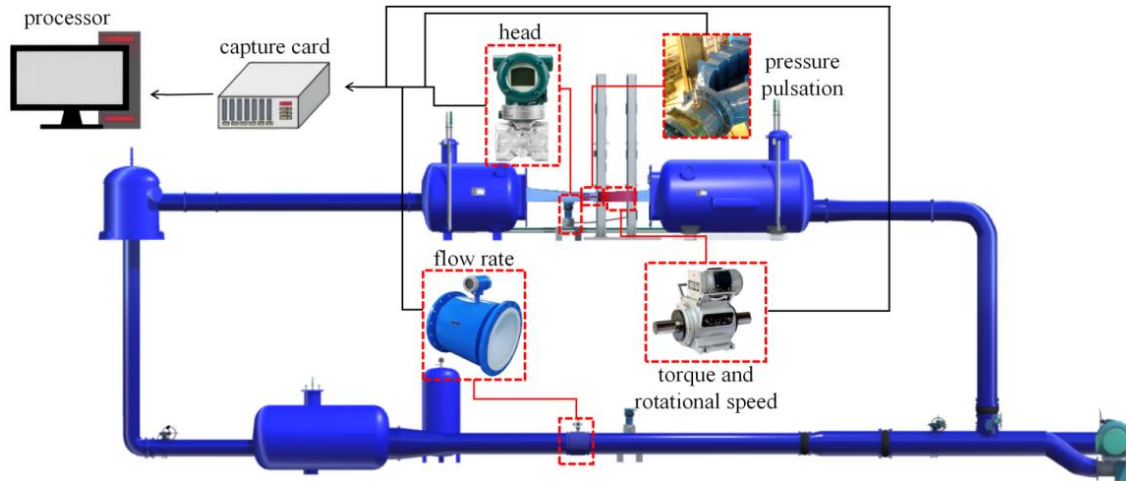
Fig. 7 High-precision hydraulic machinery test bench

satisfactory, meeting the grid convergence criterion. After considering all factors, the final grid scheme with 6483437 grid cells was selected.

3.2 Test Device and Simulation Results Verification

An assessment of the energy performance of a shaft tubular model pump device was conducted using a high-precision hydraulic equipment test bench. Figure 7 illustrates the test bench. The IMP had a 300 mm diameter with a 0.2 mm tip clearance. The measurements of head and torque were taken for scheme 1 (three IMP blades and five GVs) at different flow rates with 0° blade angle and an 981 rpm IMP speed.

The uncertainties of each equipment were verified by accredited Chinese institutions. The test bench uncertainty (±0.305%), random uncertainty (±0.206%), and comprehensive uncertainty (±0.368%) met the requirements of SL140-2006 and IEC 60193-2019, following the methodology described in reference (Yang et al., 2015). The PPS was measured using the HM90 high-frequency dynamic sensor, while signal acquisition utilized the EN900 portable rotating machinery vibration acquisition and analysis system from ENVADA Company in Beijing. The test results considered the mixed frequency amplitude of PPS at a 97% confidence level.

The analysis and comparison employed the flow coefficient (K_Q) and head coefficient (K_H), calculated using the following Eqs. (Yang & Liu, 2015):

$$K_Q = Q / (nD^3) \tag{18}$$

$$K_H = gH / (n^2D^2) \tag{19}$$
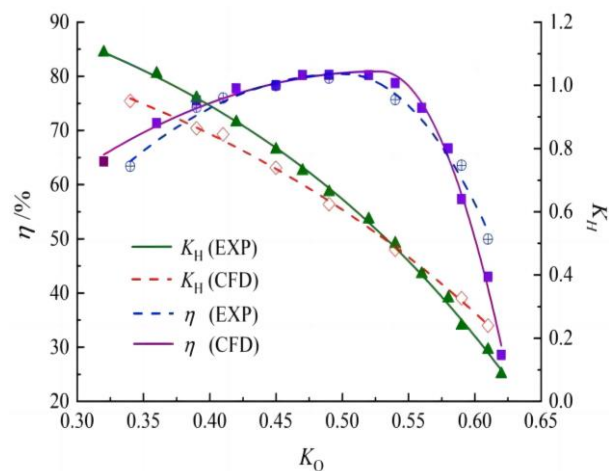
**Fig. 8 Comparison of energy performance between EXP and CFD (scheme 1)**

where Q is the flow rate, H is the head, n is the IMP rated speed, d is the nominal diameter of the IMP, and g is the acceleration of gravity.

Figure 8 presents the energy performance curve, for scheme 1. The comparison shows that the numerical simulation and test results remain consistent when the K_Q ranges from 0.34 to 0.59. The maximum K_H error is 0.04, and the maximum absolute efficiency error is 3%, indicating the strong predictive accuracy of the numerical simulation.

Table 4 shows the Reynolds numbers of the pipes at different flow rates in scheme 1. The results reveal that the flow in both pipes exhibits three-dimensional turbulence.

Table 4 Reynolds number of the pipe

	$K_Q = 0.34$	$K_Q = 0.41$	$K_Q = 0.54$
shaft inlet pipe	8.52×10^5	1.03×10^6	1.14×10^6
straight outlet pipe	8.62×10^5	9.20×10^5	1.00×10^6
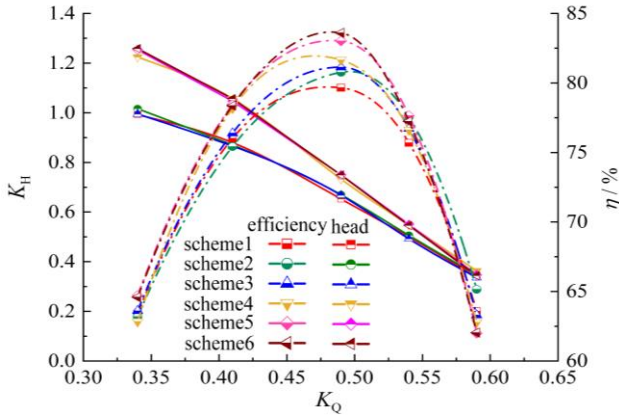
**Fig. 9 Energy performance curve of pump device**

4. RESULTS ANALYSIS AND DISCUSSION

4.1 Analysis of the Influence of Energy Performance of Pump Device

Figure 9 illustrates the energy curves under different configurations. The head of the pump appeared to be unaffected by the number of GVs, as there were only marginal differences in head values among the various GV numbers. Furthermore, there was no discernible pattern in head variations with changes in flow rate. However, an increase in IMP blades resulted in higher head values at a constant flow rate. Specifically, when the flow rate was $K_Q = 0.34$, the average relative difference between the scheme with three IMP blades and the scheme with four IMP blades was 23.6%. This difference gradually decreased as the flow rate increased. At a flow rate of $K_Q = 0.59$, the head values for different schemes tended to converge and become consistent.

The efficiency curves of shaft tubular pumps under different configurations exhibit notable differences. Figure 9 demonstrates that, in general, the shaft tubular pump was more efficient with four IMP blades compared to three blades. The efficiency difference between schemes was small at low flow rate $K_Q = 0.34$, but it increased as the flow rate rose. The maximum efficiency difference of the shaft tubular pump occurred when the flow rate approached $K_Q = 0.49$. As the flow rate continued to increase, this difference gradually decreased. At $K_Q = 0.49$, when the IMP blades was the same, schemes with more GVs exhibited higher efficiency. Overall, the efficiency followed the order of scheme 1 to scheme 6, with a maximum efficiency difference of up to 4%.

To provide further insight, relative values and absolute differences were calculated for the four flow conditions ($K_Q = 0.34$, $K_Q = 0.41$, $K_Q = 0.54$, $K_Q = 0.59$)
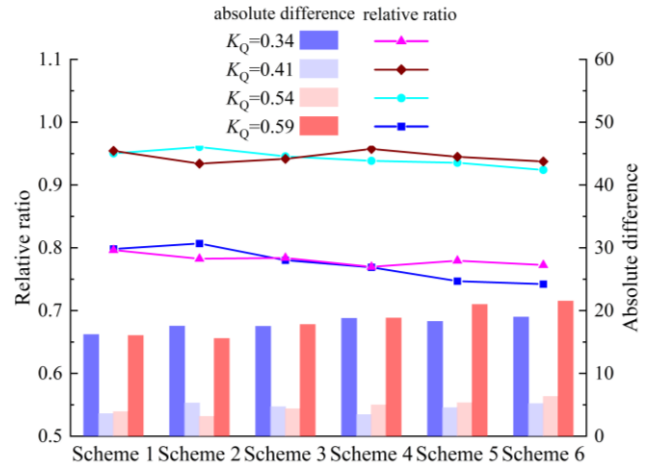
Fig. 10 Relative ratio and absolute difference of pump device efficiency

under each scheme, using the shaft tubular pump efficiency at $K_Q = 0.49$ as the reference. These results are presented in Fig. 10. For pumps with three IMP blades, scheme 2 displayed slightly lower efficiency at low flow but higher efficiency at high flow compared to schemes 1 and 3. Except at $K_Q = 0.34$, where scheme 5 exhibited higher efficiency, pumps with four IMP blades showed decreasing relative efficiency values as the number of GVs increased for all flow conditions. Overall, increasing IMP blades or the number of GVs led to larger absolute differences in the efficiency.

4.2 Flow Field Analysis of IMP and GV Coupling

The GV grooves in different schemes with varying numbers of GVs were labeled, as shown in Fig. 11. In the operation of the shaft tubular pump, an ideal GV design ensures an equal flow rate passing through each GV groove. However, due to the circulation of water flow after passing through the IMP, the actual flow rate in each GV groove often differs. Therefore, the design rationality of the schemes can be evaluated by analyzing the uniformity of flow rates in each GV groove. The Eq. for flow non-uniformity is given as:
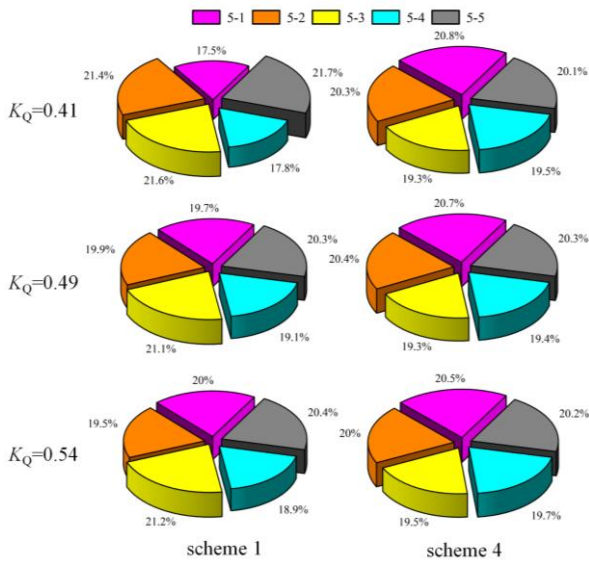
$$U' = \frac{\sqrt{\sum (Q_i - \overline{Q_i})^2}}{\overline{Q_i}} \times 100\% \tag{20}$$

where U' is the non-uniformity of flow, Q_i is the flow rate through a single GV groove, and $\overline{Q_i}$ is the average value of flow rate through each blade groove. The flow non-uniformity indicates how uneven the flow is distributed in each GV groove and its value is 0 means equal flow in all grooves.
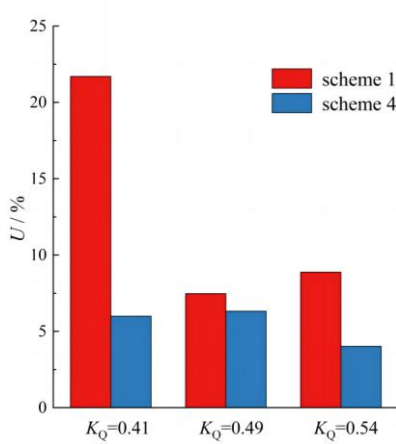

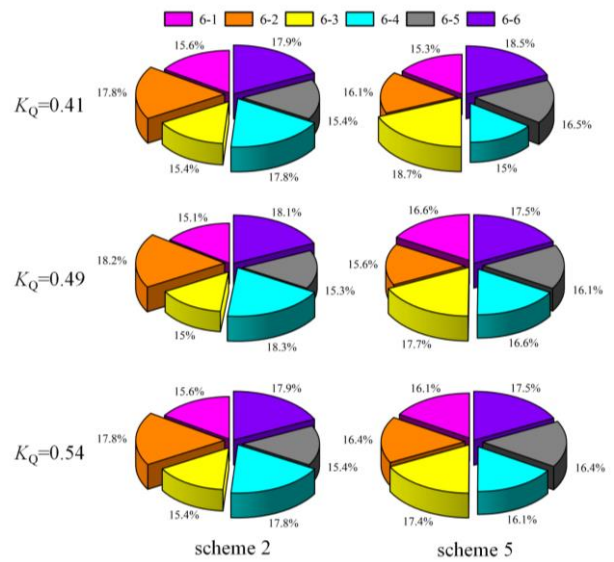**Fig. 11 GV groove number**

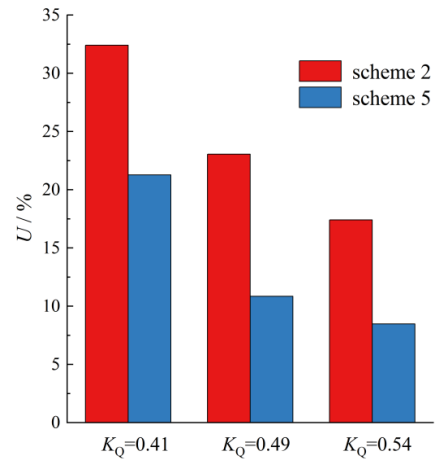(a) flow ratio

(b) flow non-uniformity

Fig. 12 The proportion of flow in each GV groove and the flow non-uniformity of the GV (5 GVs blades)

(a) flow ratio

(b) flow non-uniformity

Fig. 13 The proportion of flow in each GV groove and the flow non-uniformity of the GV (6 GVs blades)

Figure 12 shows the flow rate proportions of each GV groove and the flow non-uniformity of the GVs under different conditions ($K_Q = 0.41$, $K_Q = 0.49$, $K_Q = 0.54$) for two schemes with five GVs (scheme 1, scheme 4). The figure illustrates that, at the condition $K_Q = 0.41$, the flow distribution in each GV groove of scheme 1 is uneven. The flow rate proportions of GV groove 5-1 and 5-4 are 17.5% and 17.8%, respectively, which are lower than the average flow rate of each GV groove. In scheme 4, the uniformity of flow rates in each GV groove is significantly better than in scheme 1. The difference in flow non-uniformity is largest at the condition KQ = 0.41, followed by the condition KQ = 0.54, and the smallest at the condition KQ = 0.49. The differences in flow non-uniformity are 15.66%, 1.14%, and 4.85%, respectively.

Figure 13 illustrates the flow rate proportion of each GV groove and the flow non-uniformity of the GVs under different conditions ($K_Q = 0.41$, $K_Q = 0.49$, $K_Q = 0.54$) for two schemes with six GVs (scheme 2, scheme 5). It is evident from the figure that scheme 2 exhibits uneven flow distribution in each GV groove at all three

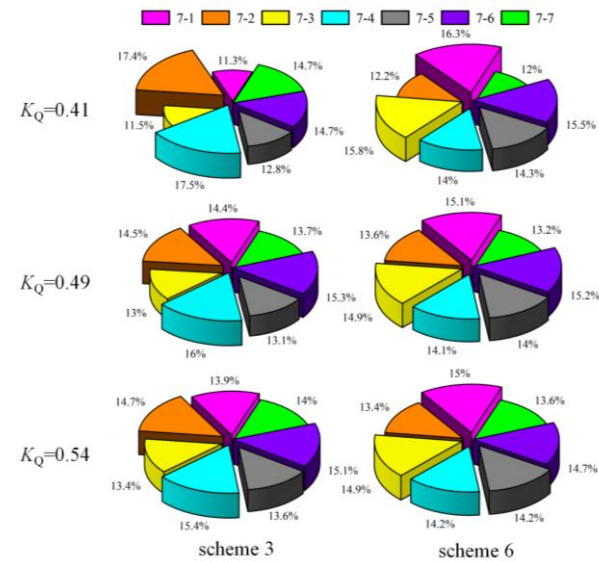conditions. GV grooves 6-1, 6-3, and 6-5 have lower flow rates, while grooves 6-2, 6-4, and 6-6 have correspondingly higher flow rates. Under scheme 5, the flow distribution in each GV groove is relatively uneven at the condition $K_Q = 0.41$. Grooves 6-1, 6-2, and 6-4 have lower flow rates, while grooves 6-3 and 6-6 have correspondingly higher flow rates. Overall, the flow non-uniformity decreases as the flow rate increases for both schemes 2 and 5. The difference in flow non-uniformity between the two schemes is greatest at the condition K_Q = 0.49, followed by $K_Q = 0.41$, and the smallest at $K_Q =$ 0.54, with values of 12.20%, 11.14%, and 8.94%, respectively.

Figure 14 presents the flow rate proportion of each GV groove and the flow non-uniformity of the GVs under different conditions ($K_Q = 0.41$, $K_Q = 0.49$, $K_Q = 0.54$) for two schemes with seven GVs (scheme 3, scheme 6). It can be observed from the figure that there is a clear uneven flow distribution in each GV groove under scheme 3 at conditions $K_Q = 0.41$ and $K_Q = 0.49$. GV grooves 7-1, 7-3, and 7-5 have lower flow rates, while
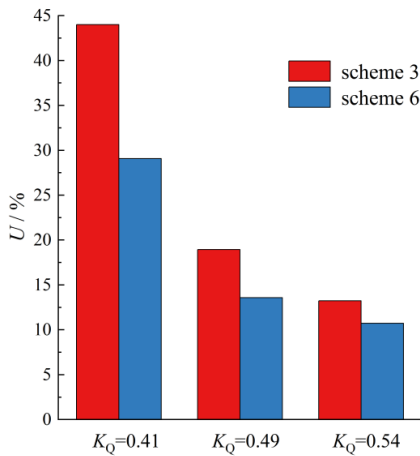
(a) flow ratio

(b) flow non-uniformity

Fig. 14 The proportion of flow in each GV groove and the flow non-uniformity of the GV (7 GVs blades)

grooves 7-2, 7-4, 7-6, and 7-7 have correspondingly higher flow rates. Under scheme 6, the flow distribution in each GV groove is relatively uneven at the condition $K_Q = 0.41$. Grooves 7-2, 7-7, and 7-4 have lower flow rates, while grooves 7-1, 7-3, and 7-6 have correspondingly higher flow rates. The overall flow non-uniformity decreases as the flow rate increases for both schemes 3 and 6. Similarly, the difference in flow non-uniformity between the two schemes decreases with increasing flow rate, with values of 14.92%, 5.37%, and 2.51%, respectively.

Figure 15 shows the average velocity circulation at the GV outlet for all six schemes. As the flow rate increases, the average velocity circulation at the outlet of the GVs also increases due to the higher flow velocity. Simultaneously, when the GV number is the same, a larger number of IMP blades leads to an increase in water flow circulation. In most cases, increasing the number of GVs helps recover more circulation created by the flow through the IMP blades. However, for scheme 5 at the condition $K_Q = 0.49$ and scheme 2 at the condition $K_Q = $
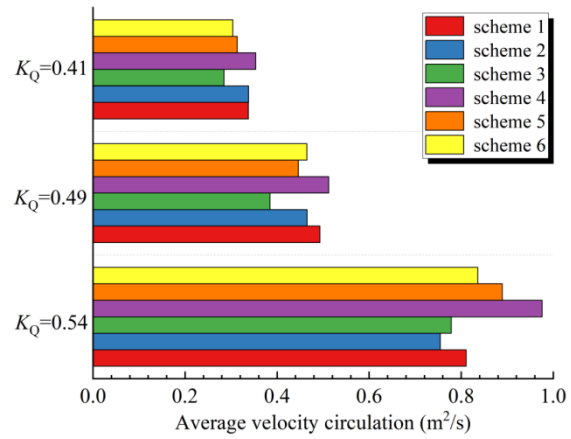
**Fig. 15 Average velocity circulation of GV outlet**

0.54, adding more GVs increases the circulation at the outlet.

Overall, increasing IMP blades from 3 to 4 leads to an increase in water flow circulation. With an increase in IMP blade number, the flow distribution becomes more equal across GV grooves, resulting in a reduction in non-uniformity by up to 17.4%. This improvement in flow distribution contributes to an overall enhancement in the pump device's efficiency. On the other hand, increasing the number of GVs tends to increase the flow non-uniformity, particularly at $K_Q = 0.41$. However, in most cases, a higher number of GVs improves their ability to recover flow circulation, leading to a decrease in average velocity circulation at the GV outlet by up to 14.3%. This improvement is beneficial for enhancing the overall efficiency.

The stability of water flow at the IMP and GV outlet section of the two schemes with the maximum efficiency difference, scheme 1 and scheme 6, was analyzed using the energy gradient. Figure 16 illustrates the K at the IMP outlet of the two schemes. The red area indicates regions with higher K function values, indicating increased turbulence intensity and poorer flow stability. At the IMP outlet, the stability of water flow decreases as the flow rate increases. Comparing scheme 1 with scheme 6, the larger IMP blades number in scheme 6 results in more unstable water flow at the IMP outlet.

Figure 17 illustrates the distribution of the K at the GV outlet. As the flow rate increases, the high K value region expands. The figure demonstrates that higher flow rates correspond to larger regions of high K values, indicating that the flow at the GV outlet becomes increasingly unstable. At the conditions $K_Q = 0.41$ and $K_Q = 0.49$, scheme 6 exhibits a significantly smaller high K value region compared to scheme 5. Combining this with the K distribution at the IMP outlet (Fig. 16), it can be inferred that the larger IMP blades number in scheme 6 provides the water flow with more energy, while the seven GVs are more effective in recovering the flow energy compared to the five GVs.
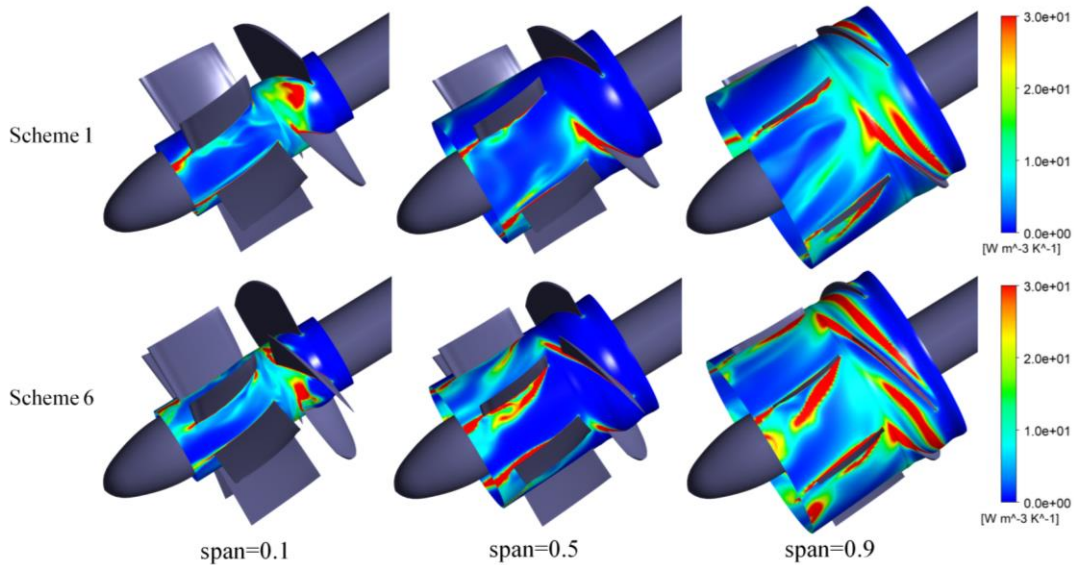
To analyze the impact of the blade number matching relationship between the IMP and GV on the internal
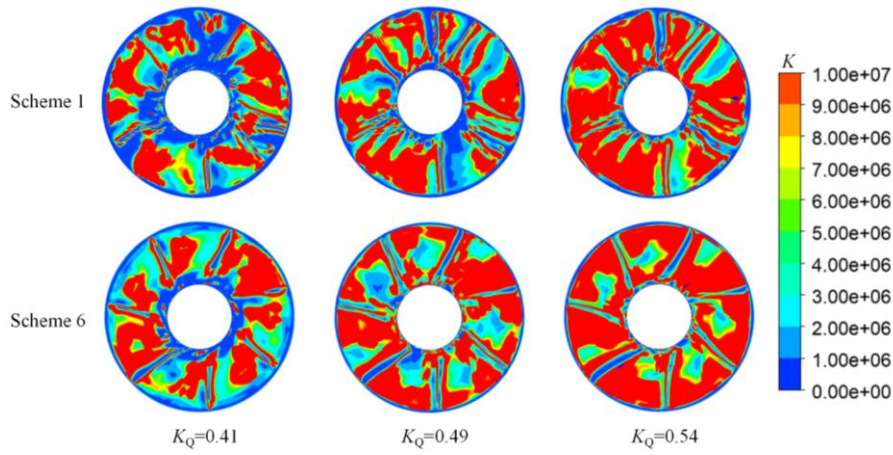
Fig. 16. Distribution of *K* at IMP outlet.
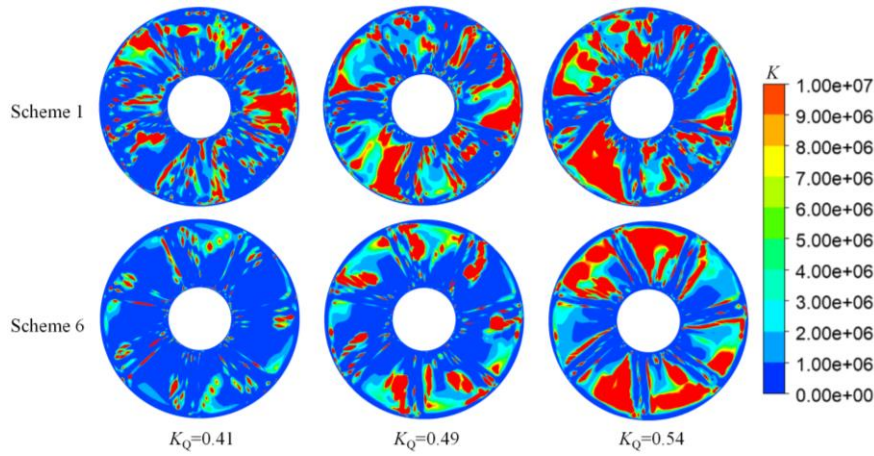
Fig. 17 Distribution of *K* at GV outlet

Fig. 18 Local EGR distribution of IMP and GV ($K_Q = 0.41$)

flow field of the pump device, schemes 1 and 6 with the maximum efficiency difference were analyzed based on entropy generation.

Figure 18 presents the distribution counter of EGR at three characteristic spans (*span* = 0.1, 0.5, and 0.9) under the condition $K_Q = 0.41$. The counter reveals strip-shaped regions of high entropy generation due to flow separation at the trailing edge (TE) of the IMP and GV and its extended area. At *span* = 0.1, there are high entropy generation regions indicating disordered flow between the IMP blades. As the number of IMP blades rises, the high entropy generation region shifts to

adjacent blade working surfaces. At *span* = 0.5, the high entropy generation region between IMP blades diminishes compared to *span* = 0.1, while the strip-shaped high entropy region at the TE of both IMP and GV expands. Scheme 6 exhibits a vortex region at the leading edge of the GVs, resulting in higher EGRs in that area. At *span* = 0.9, a distinct strip-shaped high entropy generation region appears at the leading edge of the IMP, extending tangentially. Scheme 6 produces larger regions of high entropy generation not only at the IMP's leading edge but also on the GVs, in comparison to scheme 1.

Figure 19 shows the distribution counter of EGR at three characteristic spans under the condition $K_Q = 0.49$. The counter reveals that the high entropy generation region at the TE of the IMP and GV is wider in scheme 1 than in scheme 6. At *span* = 0.1, there are high entropy generation regions between the IMP blades and near the middle of the GVs in scheme 1. At *span* = 0.5, the high entropy generation region at the TE of the IMP blades in

scheme 1 extends into the GV domain and expands in the flow direction, indicating that the disordered flow at the TE of the IMP affects the flow in the GVs. At *span* = 0.9, the local EGRs of scheme 1 and scheme 6 are roughly similar, except for slightly higher EGR near the GVs in scheme 6 compared to scheme 1.

Figure 20 shows the contour of EGR distribution at three characteristic spans under the condition $K_Q = 0.54$. At higher flow rates, the local EGR distribution patterns for the two schemes show no significant differences, indicating that the number of IMP and GVs has less influence on hydraulic losses of internal water flow in pump units under higher flow rate conditions.

The local EGR of water flow can be utilized to analyze the hydraulic loss of water flow. Under low flow rate conditions ($K_Q = 0.41$), scheme 6 exhibits a slightly higher high entropy generation region compared to scheme 1. Conversely, under the condition of $K_Q = 0.49$, scheme 1 demonstrates a larger high entropy generation
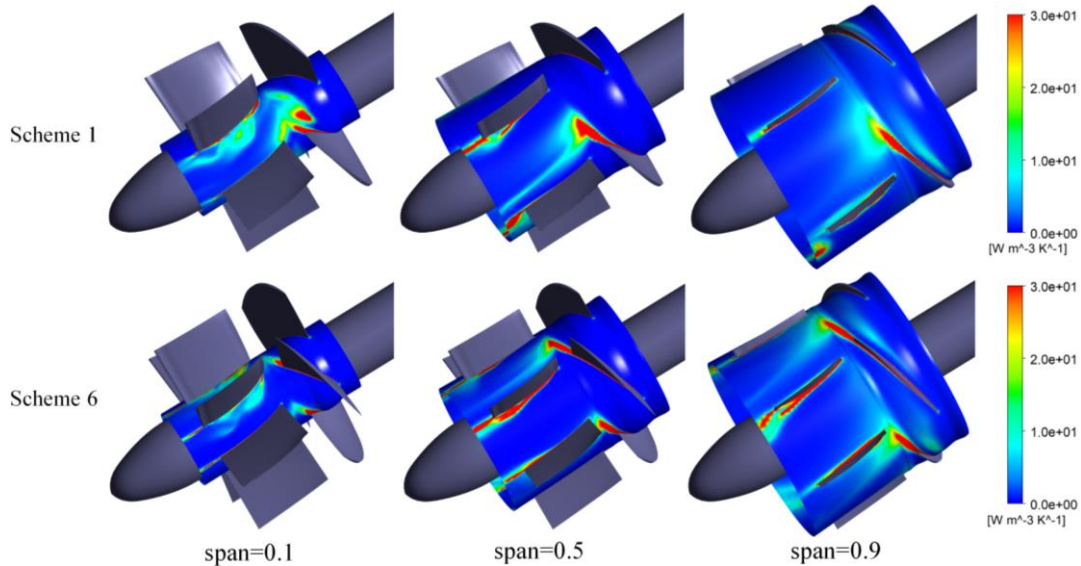
Fig. 19 Local EGR distribution of IMP and GV ($K_Q = 0.49$)
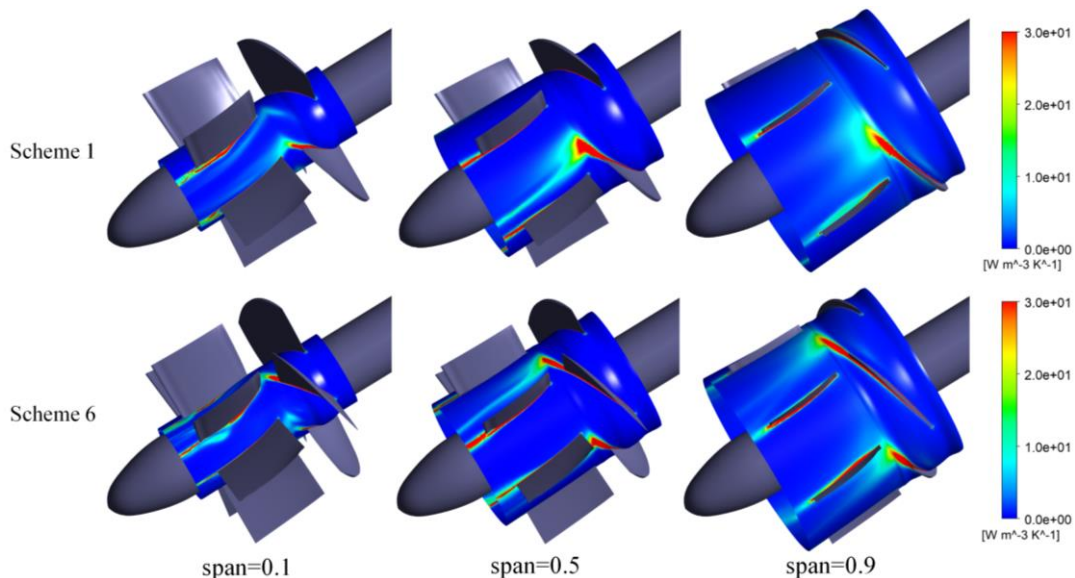
Fig. 20 Local EGR distribution of IMP and GV ($K_Q = 0.54$)
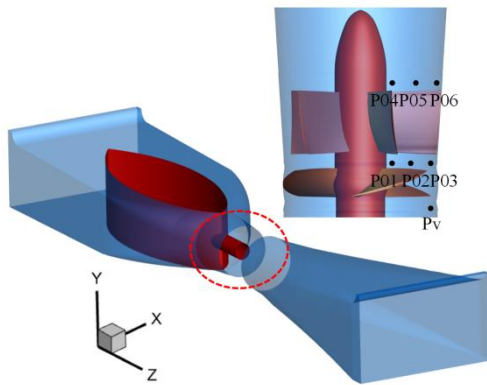
Fig. 21 PPS monitoring point arrangement

Fig. 22 Comparison of PPS spectrum between EXP and CFD (scheme 1)

region. At the condition of $K_Q = 0.54$, the entropy generation regions of the two schemes are similar. This suggests that under the condition of $K_Q = 0.49$, scheme 6 experiences lower hydraulic losses in the water flow compared to scheme 1. At this condition, the difference in efficiency between the two schemes reaches its maximum, aligning with the relationship revealed by entropy generation.

4.3 *Pressure Pulsation* Analysis *of IMP and GV*

To further investigate the effects of the blade number matching relationship between the IMP and GVs on internal pump flow PPS, PPS analyses were conducted for schemes 1 and 6. Three PPS monitoring points (Fig. 21) were positioned at the outlet of the IMP and GVs, designated as P01-P03 and P04-P06, respectively. Additionally, a monitoring point Pv was set at the inlet of the IMP for comparison and validation with PPS test data.

Time-domain analysis was performed on the PPS at the monitoring points to examine the pressure change process over time. To eliminate static pressure interference, instantaneous pressures were non-dimensionalized during time-domain analysis and converted to pressure coefficients C_p, as described by Eq. (21) (Yang et al., 2022):

$$C_p = \frac{P - \bar{P}}{0.5\rho u_2^2} \tag{21}$$

where P is the instantaneous pressure, $\bar{P}$ is the average pressure, and u_2 is the circumferential velocity.

The PPS spectrum of the test point at the upper part of the IMP inlet and the monitoring point Pv of the numerical simulation (scheme 1) were compared, as shown in Fig. 22. The figure demonstrates that the numerical simulation yielded slightly larger PPS amplitudes than the test results, but consistently predicted the primary and secondary frequencies. Overall, the trends in the numerical simulation and test results were consistent, indicating that the numerical simulation can effectively predict PPS.

Based on the energy performance and flow field analysis of scheme 1 and scheme 2, the PPS monitoring
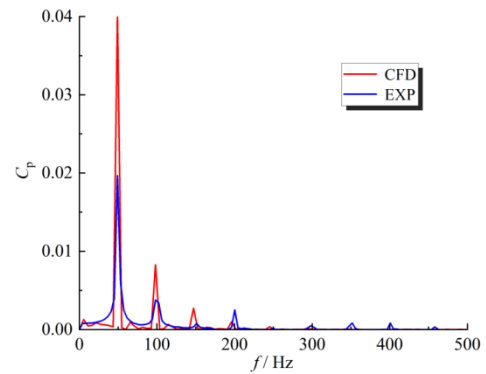
point data of the two schemes under the condition $K_Q = 0.49$ were analyzed. Figure 23 depicts the time-domain and spectral PPS at the IMP outlet for schemes 1 and 6. At the IMP outlet, the PPS of the two schemes exhibit periodic fluctuations over time, but the PPS at the monitoring points of scheme 6 are more unstable. This is evident in the larger amplitude of pressure changes over time and higher vibration amplitudes at low frequencies such as 5.4 Hz, 65.4 Hz (blade frequency), 130.8 Hz, and 196.2 Hz. On the other hand, at the IMP outlet, the PPS of scheme 1 are more stable, with a higher vibration amplitude at 49 Hz (blade frequency) compared to the vibration amplitude at the blade frequency of scheme 6.

Figure 24 illustrates the time domain and spectrum of PPS at the outlet of the GV for scheme 1 and scheme 6. The monitoring points at the GV outlet for both schemes do not exhibit obvious periodic characteristics in the time domain. The low-frequency vibration amplitude at the PPS monitoring point P04, near the hub of scheme 1, is slightly higher than that of scheme 6. There is no significant difference in the spectral characteristics at the monitoring points P05 and P06 between the two schemes.

Under the condition of $K_Q = 0.49$, the PPS characteristics of the monitoring points at the IMP outlet differ significantly between scheme 1 and scheme 6. The PPS at the monitoring points of scheme 6 are more unstable and exhibit higher vibration amplitudes at multiple low frequencies. However, the difference between the two schemes is small at the GV outlet. This indicates that while the water flow gains more energy through the IMP in scheme 6, it also results in flow instability. In scheme 6, the GV has the ability to recover the energy of the water flow, thereby aligning the PPS characteristics of the water flow with scheme 1.

5. CONCLUSION

Based on the VLES turbulence model, numerical simulations were conducted for six schemes with different blade numbers of IMP and GV. The accuracy of the simulations was verified by comparing the energy performance curves and PPS spectrum characteristics with model tests. The influence of the blade number matching relationship between the IMP and GV on the flow field was analyzed, focusing on the two schemes

(a) scheme 1

(b) scheme 6
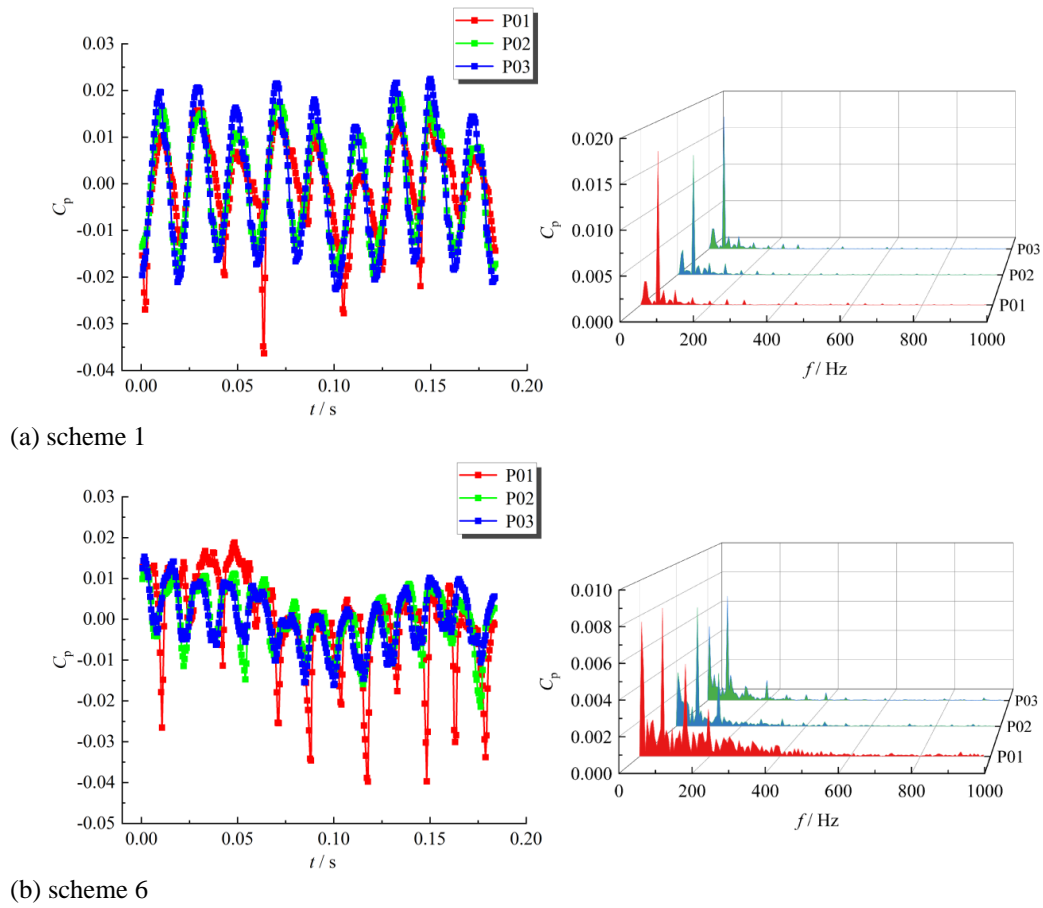
Fig. 23 Time domain and frequency spectrum of PPS at IMP outlet

(a) scheme 1

(b) scheme 6
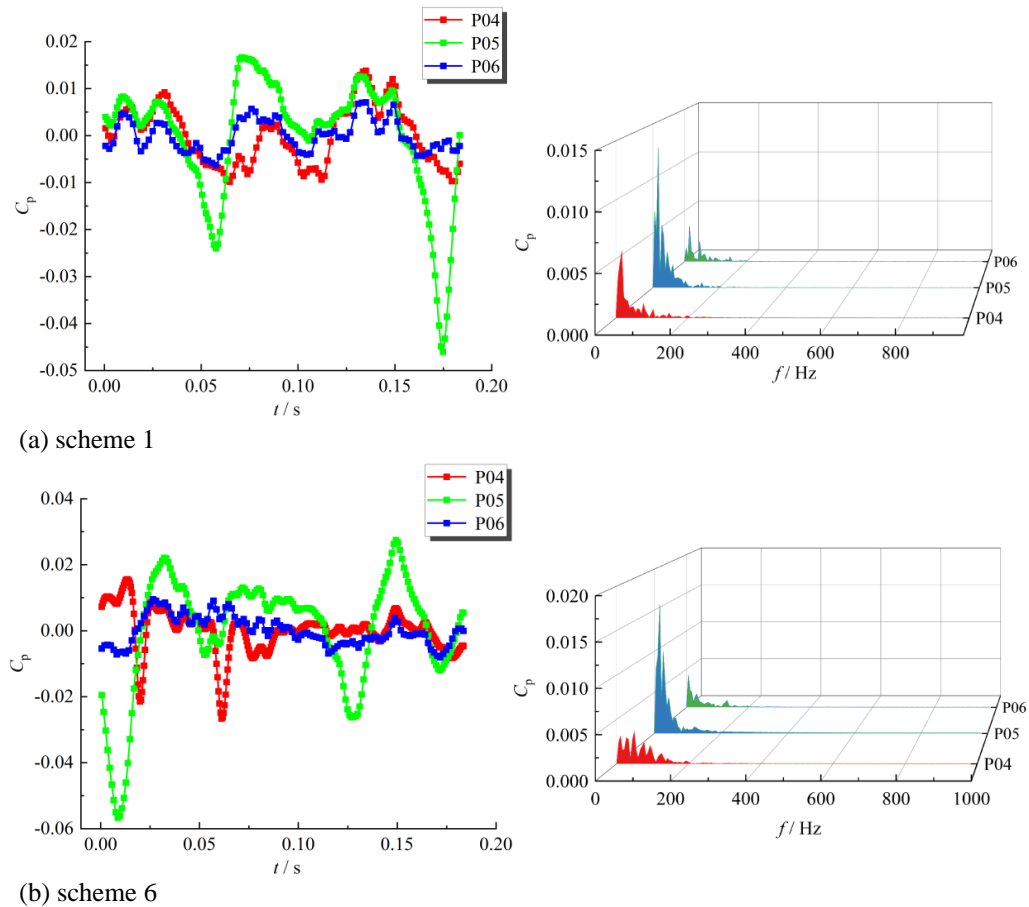
Fig. 24 Time domain and frequency spectrum of PPS at GV outlet

with the largest efficiency difference. The study explored the influence of this matching relationship on the internal steady and unsteady interference characteristics of the pump device, leading to the following conclusions:

1. Increasing the number of IMP and GV under the same flow rate condition improves pump efficiency, with the maximum influence observed at $K_Q = 0.49$. The efficiency difference between scheme 1 and scheme 6 can reach up to 4%. Pump head primarily increases with an increase in IMP blade number, and the head difference between different schemes is most pronounced at low flow rates ($K_Q = 0.34$), reaching a relative difference of 23.6%. As the flow rate rises, the pump head difference gradually decreases.

2. Increasing the IMP blade number from 3 to 4 enhances flow circulation and energy, but it also introduces water flow instability. However, an increased number of IMP blades leads to more uniform flow distribution across GV slots (reducing non-uniformity by up to 17.4%), resulting in improved overall pump efficiency. Additionally, the average circumferential outlet velocity decreases by up to 14.3% with an increase in the number of GVs, enhancing their ability to recover flow circulation and energy.

3. At $K_Q = 0.49$, the high entropy generation area of the main flow entropy generation in scheme 6 is smaller than that of scheme 1. At $K_Q = 0.54$, the entropy generation areas of the two schemes are similar. This indicates that at $K_Q = 0.49$, scheme 6 exhibits lower hydraulic losses compared to scheme 1, aligning with the efficiency difference observed in the two pump schemes.

4. At $K_Q = 0.49$, there are significant differences in the PPS characteristics of the monitoring points at the IMP outlet between scheme 1 and scheme 6. Scheme 6 shows more pronounced instability, with larger amplitude of pressure changes over time and higher vibration amplitudes at low frequencies such as 5.4 Hz, 65.4 Hz (blade frequency), 130.8 Hz, and 196.2 Hz. However, the difference between the two schemes is minimal at the GV outlet. This indicates that while scheme 6 provides more energy through the IMP, it also introduces flow instability. The GVs in scheme 6 effectively recover the water flow energy, aligning the PPS characteristics with those of scheme 1.

This study provides a detailed analysis of the rotor-stator interaction characteristics inside the pump device with respect to the matching relationship between IMP and GV. It clarifies the flow field characteristics and offers insights for designers to improve hydraulic performance and ensure stable operation during the lifecycle of the pump device. Further research is required from both experimental and theoretical perspectives to ensure the accuracy and expand the scope of this study in the future.

CONFLICT OF INTEREST

The authors declare no conflict of interest.

AUTHORS CONTRIBUTION

Conceptualization, Methodology, F. Yang; Software, Writing—Original draft & Formal analysis, Z. Lin; Writing—review and editing, X. Xu; Resources & Supervision, X. Jin; Investigation & Supervision, M. Chen; Resources & Writing—review and editing, G. Xu.

REFERENCES

Al-Obaidi, A. R. (2020). Influence of guide vanes on the flow fields and performance of axial pump under unsteady flow conditions: Numerical study. *Journal of Mechanical Engineering and Sciences*, 14(2), 6570–6593. https://doi.org/10.15282/jmes.14.2.2020.04.0516

Bejan, A. (1978). General criterion for rating heat-exchanger performance. *International Journal of Heat and Mass Transfer*, 21(5), 655–658. https://doi.org/10.1016/0017-9310(78)90064-9

Cheng, K., Li, S., Cheng, L., Sun, T., Zhang, B., & Jiao, W. (2022). Experiment on influence of blade angle on hydraulic characteristics of the shaft tubular pumping device. *Processes*, 10(3), 590. https://doi.org/10.3390/pr10030590

Dou, H. S. (2006). Mechanism of flow instability and transition to turbulence. *International Journal of Non-Linear Mechanics*, 41(4), 512–517. https://doi.org/10.1016/j.ijnonlinmec.2005.12.002

Dou, H. S., Khoo, B. C., & Yeo, K. S. (2008). Instability of Taylor–Couette flow between concentric rotating cylinders. *International Journal of Thermal Sciences*, 47(11), 1422–1435. https://doi.org/10.1016/j.ijthermalsci.2007.12.012

Han, W., Mi, J., Zhang, S., Xu, J., & Qin, B. (2021). Analysis of the influence of guide vane wrap angle and number of blades on the propulsion performance of a water-jet propeller. *International Journal of Fluid Machinery and Systems*, 14(4), 345–353. https://doi.org/10.5293/IJFMS.2021.14.4.345

Herwig, H., & Kock, F. (2006). Local entropy production in turbulent shear flows: A tool for evaluating heat transfer performance. *Journal of Thermal Science*, 15(2), 159–167. https://doi.org/10.1007/s11630-006-0159-7

Herwig, H., & Kock, F. (2007). Direct and indirect methods of calculating entropy generation rates in turbulent convective heat transfer problems. *Heat and Mass Transfer*, 43(3), 207–215. https://doi.org/10.1007/s00231-006-0086-x

Jiao, H., Sun, C., & Chen, S. (2021). Analysis of the influence of inlet guide vanes on the performance of shaft tubular pumps. *Shock and Vibration*, 2021, 1–17. https://doi.org/10.1155/2021/5177313

Kock, F., & Herwig, H. (2005). Entropy production calculation for turbulent shear flows and their implementation in cfd codes. *International Journal of Heat and Fluid Flow*, 26(4), 672–680. https://doi.org/10.1016/j.ijheatfluidflow.2005.03.005

Li, W., Ji, L., Shi, W., Yang, Y., Awais, M., Wang, Y., & Xu, X. (2020). Correlation research of rotor–stator interaction and shafting vibration in a mixed-flow pump. *Journal of Low Frequency Noise, Vibration and Active Control*, 39(1), 72–83. https://doi.org/10.1177/1461348419836530

Li, W., Liu, M., Ji, L., Wang, Y., Awais, M., Hu, J., & Ye, X. (2022a). Research on the matching characteristics of the impellers and guide vanes of seawater desalination pumps with high capacity and pressure. *Journal of Marine Science and Engineering*, 10(1), 115. https://doi.org/10.3390/jmse10010115

Li, Y., Zhong, Y., Meng, F., Zheng, Y., & Sun, D. (2022b). Entropy production analysis of a vertical mixed-flow pump device with different guide vane meridians. *Entropy*, 24(10), 1370. https://doi.org/10.3390/e24101370

Lu, Z., Tao, R., Yao, Z., Liu, W., & Xiao, R. (2022). Effects of guide vane shape on the performances of pump-turbine: A comparative study in energy storage and power generation. *Renewable Energy*, 197, 268–287. https://doi.org/10.1016/j.renene.2022.07.099

Meng, F., Pei, J., Li, Y., Yuan, S., & Cheng, J. (2017). Influence of guide vane position on hydraulic performance of bidirectional shaft tubular pump device. *Transactions of the Chinese Society for Agricultural Machinery*, 48(02), 135-140.

Nicolet, C., Ruchonnet, N., Alligné, S., Koutnik, J., & Avellan, F. (2010). *Hydroacoustic simulation of rotor-stator interaction in resonance conditions in Francis pump-turbine.* IOP Conference Series: Earth and Environmental Science. https://doi.org/10.1088/1755-1315/12/1/012005

Ohashi, H. (1994). Case study of pump failure due to rotor-stator interaction. *International Journal of Rotating Machinery*, 1, 53–60. https://doi.org/10.1155/S1023621X94000059

Pei, J., Meng, F., Li, Y., Yuan, S., & Chen, J. (2016). Effects of distance between impeller and guide vane on losses in a low head pump by entropy production analysis. *Advances in Mechanical Engineering*, 8(11), 168781401667956.

https://doi.org/10.1177/1687814016679568

Trivedi, C. (2018). Compressible large eddy simulation of a francis turbine during speed-no-load: rotor stator interaction and inception of a vortical flow. *Journal of Engineering for Gas Turbines and Power*, 140(11), 112601. https://doi.org/10.1115/1.4039423

Wang, S., Zhang, L., & Yin, G. (2017). Numerical investigation of the fsi characteristics in a tubular pump. *Mathematical Problems in Engineering*, 2017, 1–9. https://doi.org/10.1155/2017/7897614

Xie, R., Wu, Z., He, Y., Tang, F., Xie, C., & Tu, L. (2015). Study on optimization of inlet and outlet passage of bidirectional shaft tubular pump. *Transactions of the Chinese Society for Agricultural Machinery*, 46(10), 68-74.

Xu, L., Ji, D., Shi, W., Xu, B., Lu, W., & Lu, L. (2020). Influence of inlet angle of guide vane on hydraulic performance of an axial flow pump based on CFD. *Shock and Vibration*, 2020, 1–16. https://doi.org/10.1155/2020/8880789

Xu, L., Lv, F., Li, F., Ji, D., Shi, W., Lu, W., & Lu, L. (2022). Comparison of energy performance of shaft tubular pump device at two guide vane inlet angles. *Processes*, 10(6), 1054. https://doi.org/10.3390/pr10061054

Yan, J., Koutnik, J., Seidel, U., & Hübner, B. (2010). Compressible simulation of rotor-stator interaction in pump-turbines. *International Journal of Fluid Machinery and Systems*, 3(4), 315–323. https://doi.org/10.5293/IJFMS.2010.3.4.315

Yan, W., Zhu, D., Tao, R., & Wang, Z. (2022). Analysis of the flow energy loss and q-h stability in reversible pump turbine as pump with different guide vane opening angles. *Water*, 14(16), 2526. https://doi.org/10.3390/w14162526

Yang, F., & Liu, C. (2015). Numerical and experimental investigations of vortex flows and vortex suppression schemes in the intake passage of pumping system. *Advances in Mechanical Engineering*, 7(2), 547086. https://doi.org/10.1155/2014/547086

Yang, F., Li, Z., Yuan, Y., Lin, Z., Zhou, G., & Ji, Q. (2022). Study on vortex flow and pressure fluctuation in dustpan-shaped conduit of a low head axial-flow pump as turbine. *Renewable Energy*, 196, 856–869. https://doi.org/10.1016/j.renene.2022.07.024

Yang, F., Liu, C., Tang, F., & Zhou, J. (2014). Analysis of shaft profile evolution and its influence on hydraulic performance of pump device. *Journal of Basic Science and Engineering*, 22(01), 129-138.

Zhang, H., Shi, W., Chen, B., Zhang, Q., & Cao, W. (2015). Experimental study of flow field in interference area between impeller and guide vane of axial flow pump. *Journal of Hydrodynamics, Ser. B*, 26(6), 894–901. https://doi.org/10.1016/S1001-6058(14)60098-6

Zhang, N., Yang, M., Gao, B., Li, Z., & Ni, D. (2016). Investigation of rotor-stator interaction and flow unsteadiness in a low specific speed centrifugal pump. *Strojniški Vestnik - Journal of Mechanical Engineering*, 62(1), 21–31. https://doi.org/10.5545/sv-jme.2015.2859

Zhao, H., Wang, F., Wang, C., Chen, W., Yao, Z., Shi, X., Li, X., & Zhong, Q. (2021). Study on the characteristics of horn-like vortices in an axial flow pump impeller under off-design conditions. *Engineering Applications of Computational Fluid Mechanics*, 15(1), 1613–1628. https://doi.org/10.1080/19942060.2021.1985615